AFRL-RX-WP-JA-2015-0103

CONSTITUTIVE MODEL FOR ANISOTROPIC CREEP BEHAVIORS OF SINGLE-CRYSTAL Ni-BASE SUPERALLOYS IN THE LOW-TEMPERATURE, HIGH-STRESS REGIME (POSTPRINT)

Christopher Woodward, Dennis M. Dimiduk, and Michael D. Uchic
AFRL/RXCM

Yoon Suk Choi and Triplicane A. Parthasarathy
UES, Inc.

APRIL 2014
Interim Report

AIR FORCE RESEARCH LABORATORY
MATERIALS AND MANUFACTURING DIRECTORATE
WRIGHT-PATTERSON AIR FORCE BASE OH 45433-7750
AIR FORCE MATERIEL COMMAND
UNITED STATES AIR FORCE

NOTICE AND SIGNATURE PAGE

Using Government drawings, specifications, or other data included in this document for any purpose other than Government procurement does not in any way obligate the U.S. Government. The fact that the Government formulated or supplied the drawings, specifications, or other data does not license the holder or any other person or corporation; or convey any rights or permission to manufacture, use, or sell any patented invention that may relate to them.

Qualified requestors may obtain copies of this report from the Defense Technical Information Center (DTIC) (http://www.dtic.mil).

AFRL-RX-WP-JA-2015-0103 HAS BEEN REVIEWED AND IS APPROVED FOR PUBLICATION IN ACCORDANCE WITH ASSIGNED DISTRIBUTION STATEMENT.

//Signature//
_____
MICHEAL E. BURBA, Project Engineer
Metals Branch
Structural Materials Division

//Signature//
_____
DANIEL J. EVANS, Chief
Metals Branch
Structural Materials Division

//Signature//
_____
ROBERT T. MARSHALL, Deputy Chief
Structural Materials Division
Materials And Manufacturing Directorate

This report is published in the interest of scientific and technical information exchange and its publication does not constitute the Government's approval or disapproval of its ideas or findings.

REPORT DOCUMENTATION PAGE

Form Approved
OMB No. 0704-0188

1. REPORT DATE *(DD-MM-YY)*	2. REPORT TYPE	3. DATES COVERED *(From - To)*
April 2014	Interim	19 March 2014 – 31 March 2014

4. TITLE AND SUBTITLE

CONSTITUTIVE MODEL FOR ANISOTROPIC CREEP BEHAVIORS OF SINGLE-CRYSTAL Ni-BASE SUPERALLOYS IN THE LOW-TEMPERATURE, HIGH-STRESS REGIME (POSTPRINT)

5a. CONTRACT NUMBER
In-house

5b. GRANT NUMBER

5c. PROGRAM ELEMENT NUMBER
62102F

6. AUTHOR(S)

Christopher Woodward, Dennis M. Dimiduk, and Michael D. Uchic - AFRL/RXCM

Yoon Suk Choi and Triplicane A. Parthasarathy - UES, Inc.

5d. PROJECT NUMBER
4349

5e. TASK NUMBER

5f. WORK UNIT NUMBER
X0W6

7. PERFORMING ORGANIZATION NAME(S) AND ADDRESS(ES)

AFRL/RXCM
2941 Hobson Way
Bldg 654, Rm 136
Wright-Patterson AFB, OH 45433

UES Inc.
4401 Dayton-Xenia Rd.
Dayton, OH 45432-1894

8. PERFORMING ORGANIZATION REPORT NUMBER

9. SPONSORING/MONITORING AGENCY NAME(S) AND ADDRESS(ES)

Air Force Research Laboratory
Materials and Manufacturing Directorate
Wright-Patterson Air Force Base, OH 45433-7750
Air Force Materiel Command
United States Air Force

10. SPONSORING/MONITORING AGENCY ACRONYM(S)
AFRL/RXCM

11. SPONSORING/MONITORING AGENCY REPORT NUMBER(S)
AFRL-RX-WP-JA-2015-0103

12. DISTRIBUTION/AVAILABILITY STATEMENT

Distribution Statement A. Approved for public release; distribution unlimited.

13. SUPPLEMENTARY NOTES

Journal article published in *Metallurgical and Materials Transactions A*, Volume 43A, June 2012—1869. This report contains color. The final publication is available at DOI 10.1007/s11661-011-1047-7.

14. ABSTRACT

A crystallographic constitutive model is developed to capture orientation-sensitive primary and secondary creep behaviors within approximately 20 deg from the [0 0 1] orientation in single crystal superalloys for the low-temperature and high-stress regime. The crystal plasticity-based constitutive formulations phenomenologically incorporate experimentally observed dislocation micromechanisms.

15. SUBJECT TERMS

creep, nickel-based superalloy, crystal plasticity

16. SECURITY CLASSIFICATION OF:			17. LIMITATION OF ABSTRACT:	18. NUMBER OF PAGES	19a. NAME OF RESPONSIBLE PERSON (Monitor)
a. REPORT	b. ABSTRACT	c. THIS PAGE			Micheal E. Burba
Unclassified	Unclassified	Unclassified	SAR	12	19b. TELEPHONE NUMBER *(Include Area Code)* (937) 255-9795

Constitutive Model for Anisotropic Creep Behaviors of Single-Crystal Ni-Base Superalloys in the Low-Temperature, High-Stress Regime

YOON SUK CHOI, TRIPLICANE A. PARTHASARATHY, CHRISTOPHER WOODWARD, DENNIS M. DIMIDUK, and MICHAEL D. UCHIC

A crystallographic constitutive model is developed to capture orientation-sensitive primary and secondary creep behaviors within approximately 20 deg from the [0 0 1] orientation in single-crystal superalloys for the low-temperature and high-stress regime. The crystal plasticity-based constitutive formulations phenomenologically incorporate experimentally observed dislocation micromechanisms. Specifically, the model numerically delineates the nucleation, propagation, and hardening of a⟨112⟩ dislocations that shear multiple γ' precipitates by creating extended stacking faults. Detailed numerical descriptions involve slip-system kinematics from a/2⟨110⟩ dislocations shearing the γ-phase matrix, a⟨112⟩ stacking fault dislocation ribbons shearing the γ'-phase precipitate, interactions between a/2⟨110⟩ dislocations to nucleate a⟨112⟩ dislocations, and interactions between the two types of dislocations. The new constitutive model was implemented in the finite-element method (FEM) framework and used to predict primary and secondary creep of a single-crystal superalloy CMSX-4 in three selected orientations near the [0 0 1] at 1023 K (750 °C) and 750 MPa. Simulation results showed a reasonable, qualitative agreement with the experimental data. The simulation results also indicated that a/2⟨110⟩ matrix dislocations are important to limit the propagation of a⟨112⟩ dislocations, which leads to the transition to secondary creep.

DOI: 10.1007/s11661-011-1047-7

I. INTRODUCTION

SINGLE-crystal Ni-base superalloys have been an unbeatable choice for hot-section turbine blades because of their superior thermomechanical performance at increased temperatures compared with other high-temperature materials. It is generally understood that a large volume fraction of coherent cuboidal Ni_3Al-base ($L1_2$) γ'-phase precipitates regularly distributed in a Ni-base solid solution γ-phase matrix provides an excellent barrier against the motion of dislocations on thermomechanical loading. Experimental studies[1–7] show that the dislocation behavior in the γ matrix and the γ/γ' interface, and the stability of γ' precipitates vary depending on the temperature and stress, and they result in different creep behaviors for these alloys.

Near-[0 0 1] orientation (<20 deg) creep behavior of Ni-base, single-crystal superalloys has been subject to numerous experimental and numerical studies. Experimental studies[3–5] identified three distinctive near-[0 0 1] creep behaviors depending on ranges of temperature and stress. Figure 1 illustrates schematically these creep behaviors along with corresponding temperature–stress regimes based on the creep data for a second-generation Ni-base single crystal superalloy CMSX-4.[1] Other second-generation, single-crystal superalloys, such as Rene N5 and PWA1484, exhibit similar creep behaviors.[2] In Figure 1, the data points indicate stresses and temperatures at which actual creep tests were taken. Here, the data points with a same symbol indicate a similar creep behavior (or creep curves) as grouped by shaded regions. In the low-temperature, high-stress regime (LH regime in Figure 1), the deformation is dominated by primary and secondary creep. The creep strain and time for the transition from primary to secondary creep is highly sensitive to the crystallographic orientation. The magnitude of primary creep is often tied qualitatively to the degree of single slip in a particular slip system until it is hampered by latent hardening caused by activated additional slip systems.[3–7] Typically, the deformation-induced geometrical rotations are sufficient to activate additional slip systems. In the intermediate-temperature, intermediate-stress regime (MM regime in Figure 1), a typical creep curve shows an extended period of small creep strain (in the absence of primary creep) until it reaches a tertiary-creep-like stage.[3,8,9] In this regime, the gradual progression of directional coarsening (*e.g.,* rafting) of γ' precipitates is believed to be responsible for the

YOON SUK CHOI, Senior Research Scientist, and TRIPLICANE A. PARTHASARATHY, Director of Materials & Processes Division, are with the UES, Inc., Dayton, OH 45432. Contact e mail: yoon suk.choi@wpafb.af.mil CHRISTOPHER WOODWARD, Principal Materials Research Engineer, DENNIS M. DIMIDUK, Technical Director, and MICHAEL D. UCHIC, Senior Materials Research Engineer, are with the Metals Ceramics & Nondestructive Evaluation Division, Air Force Research Laboratory, AFRL/RXLM, Wright Patterson AFB, OH 45433.

Manuscript submitted August 25, 2011.
Article published online January 19, 2012

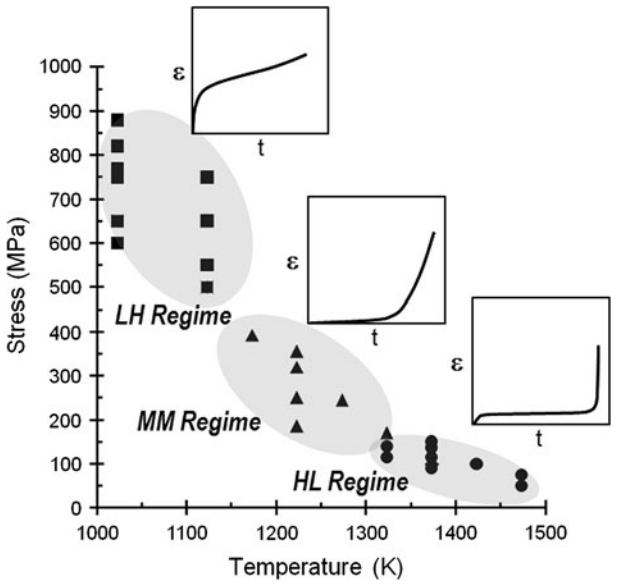

Fig. 1 Three temperature stress regimes grouped in a stress tem perature plot: Each regime represents a distinctive creep behavior, as illustrated schematically a creep curve. The classification of creep behaviors is based on the literature survey of near [0 0 1] creep of CMSX 4. All units in the schematic creep curves are arbitrary.

tertiary-dominated creep behavior as illustrated in Figure 1.[8] Creep in the high-temperature, low-stress regime (HL regime in Figure 1) typically exhibits a small amount of primary creep followed by clear secondary creep and catastrophic tertiary creep that immediately causes failure. In this regime, the completion of γ' directional coarsening is observed even in the primary creep stage, and the progression of secondary and tertiary creep is believed to be controlled by the destabilization of the γ/γ' interfacial dislocation network and the heterogeneity of inherent defects.[10 14] Note that these three distinctive creep regimes reflect different microstructural sensitivities and dislocation micromechanisms. Thus, it is imperative to incorporate those micromechanisms into a constitutive model to capture microstructure sensitivities of the creep behavior comprehensively in all stress and temperature regimes. It is the authors' long-term goal to develop a comprehensive creep constitutive model for all stress and temperature regimes.

As a first step, in the current study, we focused on developing a constitutive model that represents the orientation-sensitive primary and secondary near-[0 0 1] creep behavior in the LH regime. Significant progress has been achieved in understanding dislocation micromechanisms in this creep regime,[3 7] although a mechanistic strain-hardening law for creep has not been achieved. Creep models have also improved progressively by these pacing advances in understanding of creep mechanisms. The first part of this paper summarizes the current understanding of dislocation micromechanisms and creep models for orientation-sensitive creep in the LH regime. Distinctive features of the new creep model developed in the current study are discussed subsequently along with detailed constitutive formulations. In particular, representative microstructural features that the new creep constitutive model accounts for are clarified. Finally, creep at 1023 K (750 °C) and 750 MPa was simulated for selected loading directions (within 18 deg from the [0 0 1]), and the results are compared with the experimental creep curves for CMSX-4.

II. DISLOCATION MICROMECHANISMS AND PREVIOUS MODELS FOR NEAR-[0 0 1] CREEP IN THE LH REGIME

In the LH regime, the stress is high enough to induce γ' shearing while the temperature is still too low to facilitate directional coarsening of γ' precipitates. Experimental observations indicated that dislocations with a net Burgers vector a⟨112⟩ cut γ' precipitates by creating stacking faults (SF shearing) in a form of a superlattice intrinsic stacking fault (SISF) or a superlattice extrinsic stacking fault (SESF) in this temperature and stress regime.[3 8] Here, a/2⟨112⟩, a/3⟨112⟩, and a/6⟨112⟩ partial dislocations with a net Burgers vector a⟨112⟩ are formed in various combinations to shear γ' precipitates.[7,8] However, current constitutive models have not been developed to a sufficient state as to represent accurately the spectrum of possible a⟨112⟩-type dislocation reactions and the full fidelity of their effects on strain hardening during creep, nor has that challenge been solved by the present model. In the current work, these partial dislocation reactions are referred to as "a⟨112⟩ dislocation ribbons" without the subsequent distinction between specific dislocation reactions. Rae *et al.*[4,5,7] proposed micromechanisms for primary creep caused by SF shearing of γ' precipitates by a⟨112⟩ dislocation ribbons and the transition to secondary creep. Their primary creep mechanism involves three steps: the nucleation, propagation, and hardening of a⟨112⟩ dislocation ribbons. The nucleation of a⟨112⟩ dislocation ribbons requires a reaction of two active a/2⟨110⟩ dislocations in the γ-matrix channels or γ/γ' interfaces. Once a⟨112⟩ dislocation ribbons are nucleated, their resolved shear stresses should be high enough to percolate dislocations through γ' precipitates (in a form of mixed cutting and looping). Shearing of γ' precipitates can be done by a pair of partial dislocations (of a net Burgers vector a⟨112⟩) separated by SISF or SESF, or two pairs of partial dislocations (still of a net Burgers vector a⟨112⟩) separated by the complex stacking fault and the antiphase boundary (APB).[3,5,7] Generally, the a/2⟨110⟩ dislocations are not observed to cut γ' precipitates because an APB fault would have to be formed and then annihilated by a second coupled a/2⟨110⟩ dislocation. Here, highly orientation-sensitive primary creep in the vicinity of the [0 0 1] orientation is believed to be caused by the propagation of single a⟨112⟩ {1 1 1} slip. Suppose that orientations A and B are located in slightly different positions in the stereographic projection near the [0 0 1], as shown as open symbols in Figure 2, and a⟨112⟩{1 1 1} slip systems are operative. After applying tension stress in A and B directions, different amounts of [112](111) slip (hence, primary creep) are expected for orientations A and B

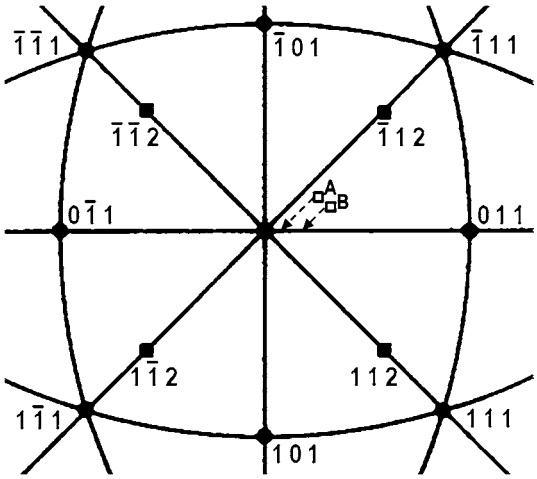

Fig. 2 Stereographic projection near [0 0 1]. The arrows indicate rotation paths of orientations A and B once the $[1\bar{1}2](\bar{1}11)$ slip system is activated under the [0 0 1] tension.

because the duration of [112](111) slip may be different between the two orientations as differing amounts of geometrical rotation (indicated by dotted arrows in Figure 2) are required to reach a multislip orientation (orientations along the [0 0 1]-[0 1 1] symmetry boundary in Figure 2). A simple dislocation percolation based calculation suggested that SF shearing of γ' precipitates by $\langle 112\rangle\{1\ 1\ 1\}$ slip produces much more shear strain (by a factor of approximately 13) compared with the case for only γ-matrix shearing by $a/2\langle 110\rangle\{1\ 1\ 1\}$ slip.[4] That estimate indicates that a relatively small difference in single $a\langle 112\rangle\{1\ 1\ 1\}$ slip duration could result in a large difference in primary creep strain. Here, single $a\langle 112\rangle\{1\ 1\ 1\}$ slip is hardened by interactions between $a\langle 112\rangle$ dislocation ribbons and $a/2\langle 110\rangle$ matrix dislocations, as well as between $a\langle 112\rangle$ dislocation ribbons from different $a\langle 112\rangle\{1\ 1\ 1\}$ slip systems.[7] This leads to the transition to secondary creep.

Now, it seems to be clear that the orientation-sensitive primary creep for crystals oriented near [0 0 1] necessitates relatively easy propagation of $a\langle 112\rangle$ dislocation ribbons throughout the entire γ/γ' microstructure. In other words, the orientation sensitivity may be less pronounced if the propagation of $a\langle 112\rangle$ dislocation ribbons is hampered effectively. This is probably the reason for different levels of orientation sensitivity of near-[0 0 1] primary creep observed for a variety of single-crystal superalloys.[6,15,16] Different compositions and heat treatments result in different values of fault energies (such as SISF and APB energies), the lattice misfit between γ and γ' phases, and different volume fractions of γ' precipitates. All these factors influence the efficiency of $a\langle 112\rangle$ dislocation ribbon propagation, hence the orientation sensitivity of near-[0 0 1] primary creep. Unfortunately, state-of-the-art constitutive modeling approaches cannot capture fully such chemistry and microstructure dependences. The current study is limited to representing primary and secondary creep behaviors phenomenologically for selected single-crystal superalloys showing highly orientation-sensitive near-[0 0 1] creep.

Early modeling of the anisotropic creep behavior near the [0 0 1] was done by Matan *et al.*[3] They proposed a phenomenological creep model, which was adopted from Gilman's dislocation density model,[17] by assuming that the mobile dislocation density directly ties to the creep strain. To capture the orientation dependence of near-[0 0 1] creep, they set the mobile dislocation attrition coefficient to be inversely proportional to θ (the rotation required to reach a multislip orientation from the original loading orientation). MacLachlan *et al.*[18 21] proposed a series of creep models for anisotropic creep of single-crystal superalloys. Their first model was a continuum damage model, which incorporated slip system kinematics to predict the anisotropic creep behavior.[18] They introduced plastic shear rates and resolved shear stresses for $a/2\langle 011\rangle$ slip and $a\langle 112\rangle$ slip, and their effective values were linked to continuum damage parameters. In addition, they used a kinematic hardening term to account for hardening contributions caused by interactions between $a/2\langle 011\rangle$ and $a\langle 112\rangle$ slip. Their first model was refined even more by enhancing softening and hardening terms for $a\langle 112\rangle$ slip and, the modified model captured the near-[0 0 1] anisotropic creep behavior of CMSX-4 at 1023 K (750 °C) and 750 MPa.[19] In their most recent model, hardening contributions from $a/2\langle 011\rangle$ slip interactions, $a\langle 112\rangle$ slip interactions, and $a/2\langle 011\rangle$-$a\langle 112\rangle$ slip interactions were treated separately.[20] This model was used to predict the creep behavior of a single-crystal turbine blade component.[21] Recently, Ma *et al.*[22] proposed an analytical creep model for the prediction of anisotropic creep for CMSX-4. They treated creep strain rates in γ matrices and γ' precipitates by $a/2\langle 011\rangle$ slip and $a\langle 112\rangle$ slip, respectively. Their creep model was based on the evolution of dislocation densities in γ matrices and γ' precipitates, as well as corresponding dislocation velocities. Major microstructural parameters, such as a width of γ-matrix channels (a volume fraction of γ' precipitates), the APB energy, and the γ/γ' lattice misfit, were incorporated in formulations of dislocation densities and velocities but not tied explicitly to slip system activation. They also incorporated an incubation effect, which is often observed in low-temperature, relatively low-stress creep, and the effect of void damage for the better prediction of primary and tertiary creep behaviors, respectively.

Generally, constitutive models for near-[0 0 1] creep in the LH regime focused on the facilitation of single $a\langle 112\rangle$ slip in the primary creep stage and latent hardening of $a\langle 112\rangle$ slip (a result of the single slip-induced geometrical rotation and the interaction with $a/2\langle 110\rangle$ γ-matrix dislocations) for the transition from primary to secondary creep. In crystal plasticity (CP) FEM, microstructural influences on single slip and strain hardening in a single crystal may be less well represented because the single-slip behavior is treated in a continuum basis, which means no discrete representation of dislocation transmission or interaction in and across precipitates in a single crystal. Because of this, constitutive models often used "flags" (in a form of hyperbolic or sinusoidal functions) to facilitate and control the single slip behavior in CP-FEM effectively.[19 21] The current

constitutive model also used those functional forms for the similar purpose.

III. NEW CONSTITUTIVE MODELING APPROACHES FOR NEAR-[0 0 1] CREEP IN THE LH REGIME

Before describing in detail the new constitutive model, it is important to clarify the representative microstructural features on which the new creep model is based. Various microstructural and defect features at different length scales may limit thermomechanical responses of single-crystal superalloys. Figure 3 shows typical microstructures of a single-crystal superalloy viewed at different length scales (magnifications). At the macroscopic scale (several millimeters to centimeters, Figure 3(a)) columnar dendrites, which are slightly misoriented relative to each other, and a colony of a few misoriented grains (freckles) may be influential features. At the intermediate scale (about a few hundred micrometers, Figure 3(b)), the chemistry gradients between dendritic cores and the interdendritic region that contains nonmetallic inclusions and microvoids are probably key features that one needs to account for. At the microscopic scale (several to tens of micrometers, Figure 3(c)), regularly distributed cuboidal γ' precipitates and surrounding γ-matrix channels are microstuctural features that control thermomechanical responses. The new creep constitutive model was developed by incorporating dislocation micromechanisms identified from electron microscopy analysis[3 7] together with certain assumptions about strain hardening. In this sense, Figure 3(c) represents the microstructural features that are represented by the current creep constitutive model. The new model has no explicit treatment of the other microstructural and defect features shown in Figures 3(a) and (b). However, dislocation behaviors in the γ/γ' microstructure (Figure 3(c)) seem to be a major factor that controls anisotropic primary and secondary creep in the LH regime, which is the focus of the current study.

In the new constitutive model, the plastic shear strain rate caused by creep deformation consists of two contributions

$$\dot{\gamma}^{\alpha} = f_{\gamma}\dot{\gamma}^{\alpha}_{m} + \dot{\gamma}^{\alpha}_{\mathrm{SF}} \qquad [1]$$

where $\dot{\gamma}^{\alpha}_{m}$ is the shear strain rate caused by the a/2⟨110⟩ dislocation activity (the slip system index α ranges from 1 to 12) in γ-matrix channels and f_{γ} is the volume fraction of the γ matrix. Also, $\dot{\gamma}^{\alpha}_{\mathrm{SF}}$ is the shear strain rate caused by shearing γ' precipitates and the γ matrix by a⟨112⟩ dislocation ribbons (α ranges from 13 to 24). Details about how constitutive formulations were developed for each of the two contributions are given in the subsequent sections.

A. $\dot{\gamma}^{\alpha}_{m}$ *Resulting from a/2⟨110⟩ Dislocations in the* γ *Matrix*

As noted previously, $\dot{\gamma}^{\alpha}_{m}$ reflects a/2⟨110⟩ dislocation behaviors in narrow γ-matrix channels. The Orowan equation was used to express $\dot{\gamma}^{\alpha}_{m}$

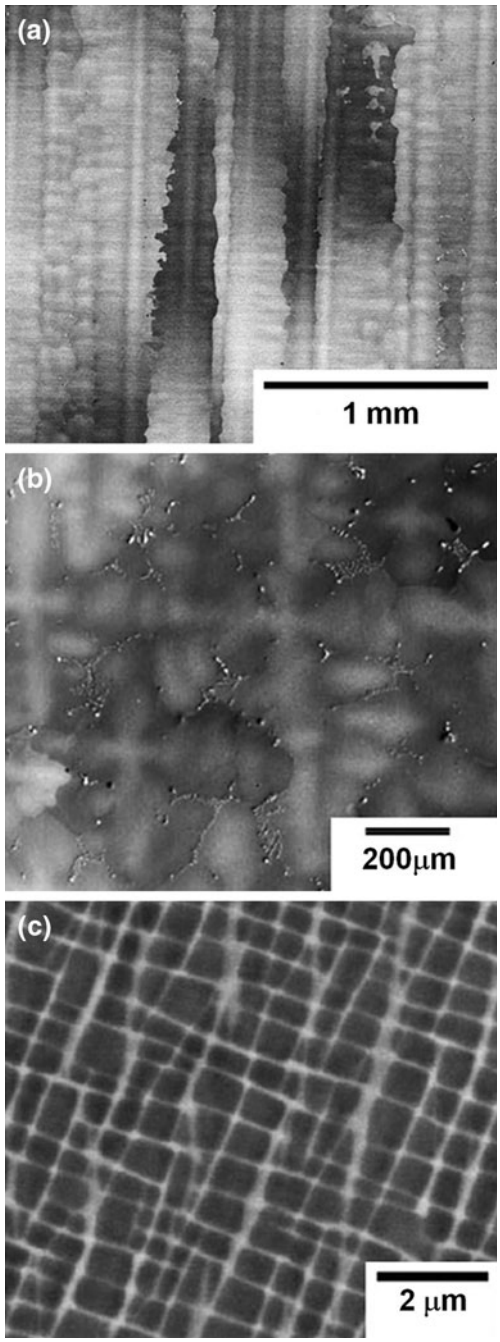

Fig. 3 Microstructural and defect features that can influence thermomechanical behaviors of single crystal superalloys at (*a*) macroscopic, (*b*) intermediate, and (*c*) microscopic length scales. All micrographs were taken from a second generation, single crystal superalloy PWA1484. The directional solidification is along the vertical direction in (a), whereas (b) and (c) are the cross sectional view.

$$\dot{\gamma}^{\alpha}_{m} = b\rho^{\alpha}_{m}v^{\alpha}_{m} \qquad [2]$$

where b, ρ^{α}_{m}, and v^{α}_{m} are the magnitude of Burgers vector, the density of a/2⟨110⟩ dislocations in the γ matrix, and the corresponding average velocity, respectively. In Eq. [2], the evolution of ρ^{α}_{m} was assumed to follow the Kocks–Mecking–Estrin equation (strain hardening law)[23,24] by

$$\dot{\rho}_m^\alpha = (k_1\sqrt{\rho_m^\alpha} - k_2\rho_m^\alpha)|\dot{\gamma}_m^\alpha| \quad [3]$$

where k_1 and k_2 are the constants that control the contributions of dislocation multiplication (hardening) and annihilation (recovery), respectively, for the evolving a/2⟨110⟩ dislocation density. In Eq. [2], a power law was adopted to describe v_m^α

$$v_m^\alpha = v_o\left|\frac{\tau_m^\alpha}{\hat{g}_m}\right|^{1/m}\text{sign}(\tau_m^\alpha) \quad [4]$$

and

$$v_o = v_o'\exp\left(-\frac{Q_m}{kT}\right) \quad [5]$$

where τ_m^α and $\hat{g}_m$ are the resolved shear stress and the slip resistance for a/2⟨110⟩ dislocations in the γ matrix, respectively, and m is the strain-rate sensitivity parameter. Also, in Eq. [5], v_o' and Q_m are the preexponent and a phenomenological activation energy for time-dependent a/2⟨110⟩ dislocation motion in the γ matrix, respectively. In this equation, the slip resistance $\hat{g}_m$ for a/2⟨110⟩ dislocations in the γ matrix was set to consist of three contributions

$$\hat{g}_m = \hat{g}_o + \hat{g}_{\text{Orowan}} + \hat{g}_{m\text{SF}} \quad [6]$$

where $\hat{g}_o$, $\hat{g}_{\text{Orowan}}$, and $\hat{g}_{m\text{SF}}$ are the slip resistances caused by the intrinsic γ-matrix strength, Orowan bowing in the γ-matrix channels, and the interaction of a/2⟨110⟩ dislocations with a⟨112⟩ dislocation ribbons, respectively. The Orowan bowing contribution $\hat{g}_{\text{Orowan}}$ was expressed by $\eta'\mu b/l$, where η', μ, and l are the geometric constant, the shear modulus, and the width of the γ-matrix channel in the {111} plane ($l = (3/2)^{1/2}l_\gamma$, where l_γ is the channel thickness), respectively. In Eq. [6], the evolution of $\hat{g}_{m\text{SF}}$ was expressed by

$$\dot{\hat{g}}_{m\text{SF}} = \sum_{\alpha=1}^{12}\sum_{\beta=13}^{24} h_{m\text{SF}}^{\alpha\beta}\dot{\gamma}_{\text{SF}}^\beta \quad [7]$$

and

$$h_{m\text{SF}}^{\alpha\beta} = h_{sm}\cdot\left(1 + \sum_{\beta=13}^{24} f_{m\text{SF}}^{\alpha\beta}\left(\frac{\tau_{\text{SF}}^\beta}{\hat{g}_{\text{SF}}^\beta}\right)\right) \quad [8]$$

where h_{sm} and $f_{m\text{SF}}^{\alpha\beta}$ are the initial hardening modulus and the coefficient for the a/2⟨110⟩ - a⟨112⟩ interaction, respectively. Also, $\dot{\gamma}_{\text{SF}}^\beta$, τ_{SF}^β, and $\hat{g}_{\text{SF}}^\beta$ are the shear rate, the resolved shear stress and the slip resistance for the ⟨112⟩{1 1 1} slip system β, respectively. Details about these three state variables will be discussed in the following section. Equations [7] and [8] were introduced to account for strengthening of the a/2⟨110⟩ slip systems because of the interaction with a⟨112⟩ dislocation ribbons.

B. *The a⟨112⟩ Dislocation Shear Rate, $\dot{\gamma}_{SF}^\alpha$*

Similar to Eq. [2], $\dot{\gamma}_{\text{SF}}^\alpha$ was expressed using the Orowan equation

$$\dot{\gamma}_{\text{SF}}^\alpha = b\rho_{\text{SF}}^\alpha v_{\text{SF}}^\alpha \quad [9]$$

where ρ_{SF}^α and v_{SF}^α are the density of a⟨112⟩ dislocation ribbons and the corresponding average velocity, respectively. In Eq. [9], the ρ_{SF}^α evolution ($\dot{\rho}_{\text{SF}}^\alpha$) and v_{SF}^α were described numerically by adopting dislocation evolution equations for the nucleation, propagation, and hardening of a⟨112⟩ SF dislocation ribbons, as proposed by Rae *et al.*[4,5,7] The evolution of ρ_{SF}^α was expressed by

$$\dot{\rho}_{\text{SF}}^\alpha = \left(k_{\text{SF}o}\rho_{\text{SF}}^\alpha M_{\text{SF}}^\alpha + k_{\text{SF1}}\frac{1}{b}\frac{1}{l_{\text{SF}}} - k_{\text{SF2}}\rho_{\text{SF}}^\alpha H_{\text{SF}}^\alpha\right)|\dot{\gamma}_{\text{SF}}^\alpha| \quad [10]$$

where $k_{\text{SF}o}$, k_{SF1}, and k_{SF2} are the constants that control the contribution of the corresponding terms. Equation [10] basically incorporates the nucleation, propagation, and immobilization of a⟨112⟩ dislocation ribbons.

The first term of the right-hand side (RHS) of Eq. [10] accounts for the production of the a⟨112⟩ dislocation density because of the nucleation of a⟨112⟩ dislocation ribbons from the reaction of two a/2⟨110⟩ dislocations in the γ matrix and the γ/γ' interface.[7] Table I shows a list of slip systems for a/2⟨110⟩ slip and a⟨112⟩ slip along with the corresponding notations.

The reaction of two a/2⟨110⟩{1 1 1} slip systems can produce the a ⟨112⟩{1 1 1} slip system if the resulting ⟨112⟩ vector and ⟨110⟩ vector lie in the same {1 1 1} plane. Based on this reaction criterion, Table II lists possible a⟨112⟩{1 1 1} slip systems from reactions of two a/2⟨110⟩{1 1 1} slip systems.

Because the reaction matrix in Table II is symmetric, only a diagonal half of the reaction matrix needs to be considered. Here, one can notice from Table II that each a⟨112⟩{1 1 1} slip system can be produced by three different pairs of a/2⟨110⟩{1 1 1} slip systems. This finding implies that the availability of nucleating each of a⟨112⟩{1 1 1} slip system can be checked by examining activities of the corresponding three pairs of a/2⟨110⟩{1 1 1} slip systems. Thus, the nucleation term in Eq. [10] is completed by introducing M_{SF}^α to quantify the availability of the a⟨112⟩{1 1 1} nucleii

$$M_{\text{SF}}^\alpha = \left(\max_{i=1,2,3}\left\{\left|\frac{\tau_m^{\min(a_i,b_i)}}{\tau_m^{\max(a_i,b_i)}}\right|\cdot\left|\tau_m^{\text{avg}(a_i,b_i)}\right|\right\}\frac{1}{|\hat{\tau}_{\text{SF}}|} - M_o\right)\frac{1}{R_M} \quad [11]$$

Table I. Twelve a/2⟨110⟩{1 1 1} and Twelve a⟨112⟩{1 1 1} Slip Systems and Their Notations

⟨110⟩{1 1 1}	⟨112⟩{1 1 1}
A1 [011](111)	A I [112](111)
A2 [101](111)	A II [12$\bar{1}$](111)
A3 [110](111)	A III [2$\bar{1}$1](111)
B1 [0$\bar{1}$1](111)	B I [11$\bar{2}$](111)
B2 [$\bar{1}$01](111)	B II [$\bar{1}$2$\bar{1}$](111)
B3 [$\bar{1}$10](111)	B III [$\bar{2}$11](111)
C1 [011](11$\bar{1}$)	C I [112](11$\bar{1}$)
C2 [101](11$\bar{1}$)	C II [12$\bar{1}$](11$\bar{1}$)
C3 [110](11$\bar{1}$)	C III [211](11$\bar{1}$)
D1 [0$\bar{1}$1](11$\bar{1}$)	D I [11$\bar{2}$](11$\bar{1}$)
D2 [101](11$\bar{1}$)	D II [121](11$\bar{1}$)
D3 [110](11$\bar{1}$)	D III [2$\bar{1}$1](11$\bar{1}$)

Table II. The Matrix Showing Output a⟨112⟩{1 1 1} Slip Systems from Reactions of Two a/2⟨110⟩{1 1 1} Slip Systems

	A1	A2	A3	B1	B2	B3	C1	C2	C3	D1	D2	D3
A1		A I	A II		B I	B II		A I				A II
A2	A I		A III	A I			C I		C III			A III
A3	A II	A III		A II				A III		D II	D III	
B1		A I	A II		B I	B II			B II		B I	
B2	B I			B I		B III			B III	D I		D III
B3	B II			B II	B III		C II	C III			B III	
C1		C I				C II		C I	C II		D I	D II
C2	A I		A III			C III	C I		C III	C I		
C3		C III		B II	B III		C II	C III		C II		
D1			D II		D I			C I	C II		D I	D II
D2			D III	B I		B III	D I			D I		D III
D3	A II	A III			D III		D II			D II	D III	

where for each of a⟨112⟩{1 1 1} slip systems (α = 13 to 24 in Eq. [11]), the index i indicates three available pairs of a/2⟨110⟩{1 1 1} slip systems and $\tau_m^{\min(a_i,b_i)}$, $\tau_m^{\max(a_i,b_i)}$, and $\tau_m^{\text{avg}(a_i,b_i)}$ are the smaller, larger, and average resolved shear stresses for each a/2⟨110⟩{1 1 1} pair, respectively. Also, $\hat{\tau}_{SF}$ is the stress required to create a stacking fault ($\hat{\tau}_{SF} = \eta_{SF} E_{SF}/b$, where η_{SF} and E_{SF} are the constant and the stacking fault energy in the γ matrix, respectively), and M_o and R_M are constants. The first term of the RHS of Eq. [11] was formulated such that the nucleation of the a⟨112⟩{1 1 1} comes from a most active a/2⟨110⟩{1 1 1} pair by checking the corresponding interactions in Table II. In Eq. [11], the second term M_o was intended to cut off the value range of the first term before the normalization by R_M.

The second term of the RHS of Eq. [10] is intended to incorporate the multiplication of a⟨112⟩ dislocation ribbons. Here, l_{SF} is the average γ' SF-shearing distance ($l_{SF} = (L^2/(3)^{1/2})^{1/2}$, where L is the size of the cuboidal γ' precipitate[25]). The third term of the RHS of Eq. [10] accounts for the immobilization of a⟨112⟩ dislocation ribbons by interactions between different a⟨112⟩ dislocation ribbons. The law governing the immobilization follows a modified Kock, Argon, and Ashby form that accounts for the maximally stressed a⟨112⟩{1 1 1} glide system. Here, H_{SF}^{α} was expressed by

$$H_{SF}^{\alpha} = 1 - \exp\left[-\left(\max_{\substack{\beta=13\ldots24\\ \beta\neq\alpha}}\left\{f_{SF}^{\alpha\beta}\left|\frac{\tau_{SF}^{\beta}}{\tau_{SF}^{\max}}\right|\cdot\left|\tau_{SF}^{\text{avg}(\alpha,\beta)}\right|\right\}\frac{1}{\left|\tau_{SF}^{\max}\right|} + p_{SF}\right)^{q_{SF}}\right] \quad [12]$$

In Eq. [12], $f_{SF}^{\alpha\beta}$ is the interaction coefficient, and p_{SF} and q_{SF} are constants. Also, $\tau_{SF}^{\max}$ is the maximum resolved shear stress of all a⟨112⟩{1 1 1} slip systems, and $\tau_{SF}^{\text{avg}(\alpha,\beta)}$ is the average resolved shear stress of the two a⟨112⟩{1 1 1} slip systems. Equation [12] was formulated in such a fashion so that rapid immobilization (in a form of an S-type curve) of the primary slip system takes place as the secondary slip system becomes active.

Returning to Eq. [9], the average velocity of a⟨112⟩ dislocation ribbons was expressed using a power law as

$$v_{SF}^{\alpha} = v_{SFo}\left|\frac{\tau_{SF}^{\alpha}}{\hat{g}_{SF}}\right|^{1/m_{SF}}\text{sign}(\tau_{SF}^{\alpha}) \quad [13]$$

and

$$v_{SFo} = v'_{SFo}\exp\left(-\frac{Q_{SF}}{kT}\right) \quad [14]$$

where m_{SF} is the strain rate sensitivity parameter. Also, in Eq. [14], v'_{SFo} and Q_{SF} are the preexponent and the activation energy for a⟨112⟩ dislocations, respectively. Here, the slip resistance $\hat{g}_{SF}^{\alpha}$ for a⟨112⟩ dislocation ribbons was set to originate from two contributions

$$\dot{\hat{g}}_{SF}^{\alpha} = h_{SF}^{\alpha}\dot{\gamma}_{SF}^{\max} + \sum_{\beta=1}^{12} h_m^{\alpha\beta}\dot{\gamma}_m^{\beta} \quad [15]$$

The first and second terms of the RHS of Eq. [15] are hardening contributions from a⟨112⟩ - a⟨112⟩ interactions and from a⟨112⟩ - a/2⟨110⟩ interactions, respectively. The initial value of $\hat{g}_{SF}^{\alpha}$ was determined by $\hat{g}_{SF}^{\alpha} = E_{APB}/b$, where E_{APB} is the APB energy for γ' precipitates. In Eq. [15], $\dot{\gamma}_{SF}^{\max}$ is the maximum shear rate of a⟨112⟩{1 1 1} slip systems. Here, h_{SF}^{α} is the hardening modulus from a⟨112⟩ - a⟨112⟩ interactions and was expressed by

$$h_{SF}^{\alpha} = \left(h_s\cdot\text{sech}^{1/2}\left(\frac{\gamma_{SF}^{\alpha}}{\gamma_1}\right)\right)\cdot\left(1 + n_{SF}H_{SF}^{\alpha}\right) \quad [16]$$

where h_s and γ_1 are the initial hardening modulus and the normalization constant, respectively. Also, n_{SF} is the scaling constant that links H_{SF}^{α} of Eq. [12] to h_{SF}^{α}. For the second term in Eq. [15], $h_m^{\alpha\beta}$ is the hardening modulus stemming from a⟨112⟩ - a/2⟨110⟩ interactions that was expressed by

$$h_m^{\alpha\beta} = h_{SFm}\cdot\left(1 + \sum_{\beta=1}^{12} f_m^{\alpha\beta}\tanh\left(\frac{\gamma_m^{\beta}}{\gamma_{SF}^{\max}}\right)\right) \quad [17]$$

where h_{SFm} and $f_m^{\alpha\beta}$ are the initial hardening modulus and the coefficient for a⟨112⟩ - a/2⟨110⟩ interactions, respectively.

IV. SIMULATION OF ANISOTROPIC CREEP FOR CMSX-4

The new constitutive model described in the previous section was used to capture orientation sensitivity of near-[0 0 1] creep of a single-crystal superalloy CMSX-4. All constitutive formulations (Eqs. [1] to [17]) were implemented in the commercial FEM package ABAQUS (Simulia, Providence, RI) through the user material subroutine (UMAT). Here, a tangent modulus method[26] was adopted for the time integration. Preliminary parametric studies were performed to identify reasonable ranges for values of major input parameters. Table III lists values of input parameters for the description of $\dot{\gamma}_m^{\alpha}$ and $\dot{\gamma}_{SF}^{\alpha}$.

In Table III, the values of parameters marked with the asterisk were determined by fitting to the creep data in Figure 5.[3] The values for activation energies (Q_m and Q_{SF}) and fault energies (E_{APB} and E_{SF}) were approximated from the experimental and modeling data.[27 30] The values for l_γ, f_γ, L and b were directly taken from the input microstructure (cuboidal γ' precipitates with an edge length of 0.52 μm and the volume fraction of 68 pct). The constants in Eqs. [3] and [10], and the parameters in Eqs. [4] and [13] were determined from a range of values used in other models.[31 33] The geometric constants η' and η_{SF} were set as 1 for the current simulations. Also, the coefficients (f_{mSF}, f_m, and f_{SF}) for the interaction of different slip mechanisms were assumed to be 1 because their values are not informed. The shear modulus μ was calculated from $\mu = [0.5 \cdot C_{44} \cdot (C_{11} - C_{12})]^{1/2}$, where the temperature dependence of elastic constants (C_{11}, C_{12}, and C_{44}) for CMSX-4 was determined by experimental fits from Allan.[34] Figure 4(a) shows the sample geometry used for FEM simulations. A cylindrical sample was meshed by the combination of linear wedge (C3D6) and brick (C3D8) elements. Boundary conditions for creep deformation were applied to the meshed sample by restraining the bottom face vertically and applying appropriate body forces to the top mesh layer of the cylindrical sample to induce an axial stress comparable with the creep stress. Figure 4(b) shows the contour of accumulated shear in the deformed sample geometry after 15 pct creep strain along the single slip-oriented direction. One can observe that the deformed geometry is locally nonuniform, which is typical for single crystals deformed in low symmetry (*viz.*, single slip oriented) orientations.

Using the new constitutive model described in Section III and the sample geometry shown in Figure 4(a), the creep simulations were performed in three different crystallographic directions near the [0 0 1] at 1023 K (750 °C) and 750 MPa, and the resulting creep curves were compared with those from CMSX-4[3] in Figure 5. Here, three creep orientations K, L, and M are misoriented from the [0 0 1] by 5.3, 8.0, and 17.5 deg, respectively. The prediction result (Figure 5) confirms that the new creep constitutive model reasonably the orientation sensitivity of primary and secondary creep captures for near-[0 0 1] oriented single-crystal superalloys. In Figure 6, the shear strain rates from a$\langle 112 \rangle$ slip ($\dot{\gamma}_{SF}$) and a/2$\langle 110 \rangle$ matrix slip ($\dot{\gamma}_m$) were averaged over an entire sample volume and plotted as a function of creep time. As expected, a$\langle 112 \rangle$ slip dominates for all three orientations, and the degree of primary creep is shown to be inversely proportional to the level of the $\dot{\gamma}_{SF}$ suppression, which is highest in M and lowest in K. Here, it is interesting to note that $\dot{\gamma}_m$ shows the opposite trend, the highest suppression in K and the lowest suppression in M. Importantly, this result implies that a/2$\langle 110 \rangle$ matrix slip cannot be ignored, and it plays an important role in blocking a$\langle 112 \rangle$ dislocation ribbons slip activities effectively, leading to the transition to secondary creep. The current simulation results seem to

Table III. Values of Input Parameters Used for the Current Simulations

$\dot{\gamma}_m^{\alpha}$		$\dot{\gamma}_{SF}^{\alpha}$			
Q_m	323 kJ/mol	Q_{SF}	280 kJ/mol	M_o	0.4*
$\hat{g}_o$	300 MPa*	E_{APB}	0.12 J/m^2	R_M	0.3*
k_1	1.2×10^8/m	E_{SF}	0.11 J/m^2	h_s	40 GPa*
k_2	30	k_{SFo}	4	γ_1	0.07*
v_o'	1×10^9/s	k_{SF1}	2×10^{-4}	n_{SF}	24*
m	0.13	k_{SF2}	2	h_{SFm}	10 GPa*
η'	1	v'_{SFo}	1×10^9/s	f_m	1
l_γ	0.068×10^{-6} m	m_{SF}	0.25	f_{SF}	1
h_{sm}	10 GPa*	η_{SF}	1	p_{SF}	0.028*
f_{mSF}	1	L	0.52×10^{-6} m	q_{SF}	250*
f_γ	0.32	k_{SFo}	4		
b	2.489 Å				

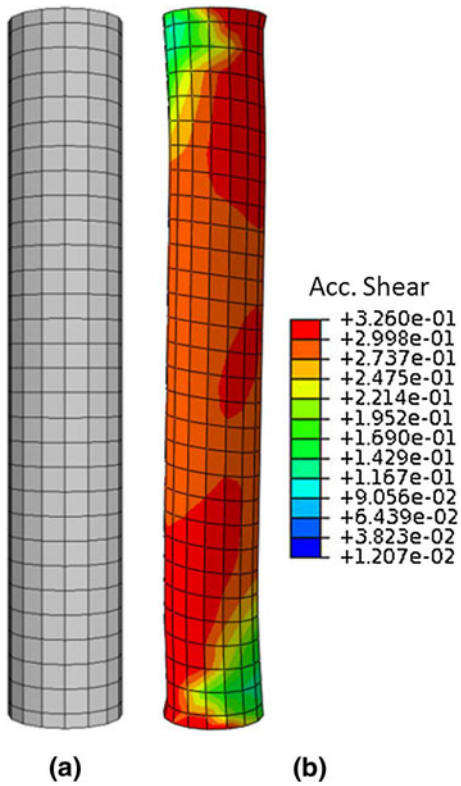

Fig. 4 (*a*) A cylindrical sample geometry meshed by linear wedge (C3D6) and brick (C3D8) elements. (*b*) The contour of accumulated shear in the deformed sample geometry after 15 pct creep strain in a single slip oriented direction.

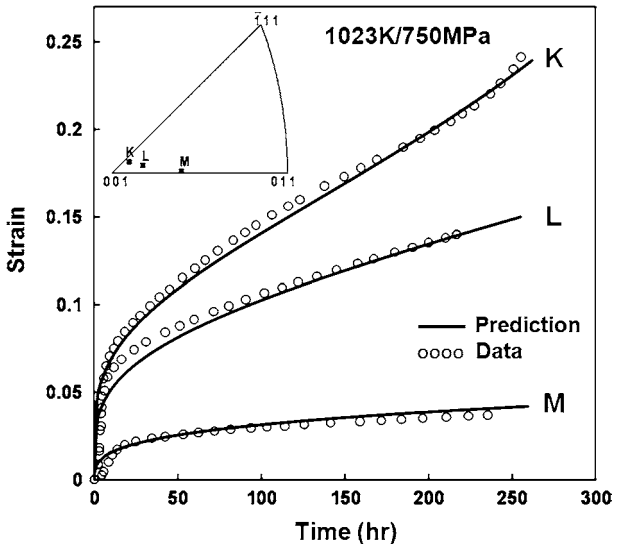

Fig. 5 Creep curve comparison between predictions (solid curves) and CMSX 4 data (circles): three creep loading directions K, L, and M are indicated in a crystallographic triangle. Experimental creep curves were taken from Ref. 3.

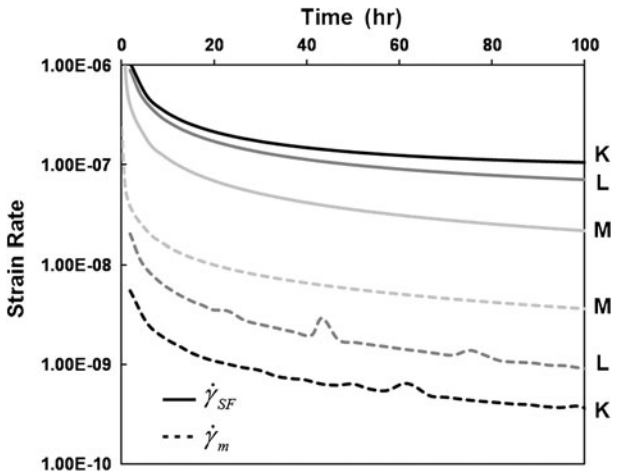

Fig. 6 Average shear strain rates from a⟨112⟩ SF slip ($\dot{\gamma}_{SF}$, solid lines) and a/2⟨110⟩ matrix slip ($\dot{\gamma}_m$, broken lines) plotted as a function of creep time for orientations K, L, and M.

be in agreement with conclusions of experimental studies that emphasized the importance of a/2⟨110⟩ matrix dislocations to control a⟨112⟩ slip propagation.[4,6]

V. CONCLUDING REMARKS

The current study developed a new crystallographic constitutive model to predict highly anisotropic primary and secondary creep near the [0 0 1] orientation of single-crystal superalloys in relatively low-temperature and high-stress ranges. Crystal plasticity formulations using slip systems kinematics were developed, guided by experimentally observed dislocation micromechanisms. The new constitutive model captured the experimental creep behavior of near-[0 0 1] oriented CMSX-4 reasonably. It suggests that crystal plasticity is a reasonable framework that can be used to capture primary and secondary creep of single-crystal superalloys in the low-temperature and high-stress regime. The simulation results also suggest that in addition to a⟨112⟩ - a⟨112⟩ interactions, a/2⟨110⟩ matrix dislocations are responsible for limiting the propagation of a⟨112⟩ dislocation ribbons by a⟨112⟩ - a/2⟨110⟩ interactions. This was in agreement with the suggestion made by experimental studies.

ACKNOWLEDGMENT

This work was supported initially by AVETEC, Springfield, OH through the AFOSR NALI program (Program Manager: Dr. J. Tiley of AFRL/RXLM). The authors are grateful to Drs. R. Dutton, S. Russ, and A. Rosenberger of AFRL/RXL for various supports throughout the project. Support from the AFRL/RXLM under contract # FA8650-10-D-5226 is acknowledged by Y.S.C. and T.A.P. Computations were performed using computer resources at the Ohio Supercomputer Center (grant no. PAS0647, Professor G. Daehn of The Ohio State University). This research was also supported in part by a grant of computer resources at the AFRL-DSRC.

REFERENCES

1. R.C. Reed: *The Superalloys: Fundamentals and Applications*, Cambridge Press, Cambridge, UK, 2006, pp. 171 87.
2. Y. Koizumi, T. Yokokawa, H. Harada, and T. Kobayashi: *J. Japan Inst. Met.*, 2006, vol. 70, pp. 176 79.
3. N. Matan, D.C. Cox, P. Carter P, M.A. List, C.M.F. Rae, and R.C. Reed: *Acta Mater.*, 1999, vol. 47, pp. 1549 63.
4. C.M.F. Rae, N. Matan, D.C. Cox, M.A. Rist, and R.C. Reed: *Metall. Mater. Trans. A*, 2000, vol. 31A, pp. 2219 28.
5. C.M.F. Rae, N. Matan, and R.C. Reed: *Mater. Sci. Eng. A*, 2001, vol. 300, pp. 125 34.
6. G.L. Drew, R.C. Reed, K. Kakehi, and C.M.F. Rae: *Superalloys 2004*, K.A. Green, T.M. Pollock, H. Harada, T.E. Howson, R.C. Reed, J.J. Schirra and S. Walston, eds., TMS, Warrendale, PA, 2004, pp. 127 36.
7. C.M.F. Rae and R.C. Reed: *Acta Mater.*, 2007, vol. 55, pp. 1067 81.
8. V.A. Vorontsov, C. Shen, Y. Wang, D. Dye, and C.M.F. Rae: *Acta Mater.*, 2010, vol. 58, pp. 4110 19.
9. N. Matan, D.C. Cox, C.M.F. Rae, and R.C. Reed: *Acta Mater.*, 1999, vol. 47, pp. 2031 45.
10. R.C. Reed, N. Matan, D.C. Cox DC, M.A. List MA, and C.M.F. Rae: *Acta Mater.*, 1999, vol. 47, pp. 3367 81.
11. A. Epishin and T. Link: *Phil. Mag.*, 2004, vol. 84, pp. 1979 2000.
12. T. Link, A. Epishin, M. Klaus, U. Bruckner, and A. Reznicek: *Mater. Sci. Eng. A*, 2005, vol. 405, pp. 254 65.
13. Z.X. Zhang, J.C. Wang, H. Harada, and Y. Koizumi: *Acta Mater.*, 2005, vol. 53, pp. 4623 33.
14. P.M. Sarosi, R. Srinivasan, G.T. Eggeler, M.V. Nathal, and M.J. Mills: *Acta Mater.*, 2007, vol. 55, pp. 2509 18.
15. R.C. Reed, D.C. Cox, and C.M.F. Rae: *Mater. Sci. Eng. A*, 2007, vol. 448, pp. 88 96.
16. D.M. Shah, S. Vega, S. Woodard, and A.D. Cetel: *Superalloys 2004*, K.A. Green, T.M. Pollock, H. Harada, T.E. Howson, R.C. Reed RC, J.J. Schirra, and S. Walston, eds., TMS, Warrendale, PA, 2004, pp. 197 206.
17. J.J. Gilman: *Micromechanics of Flow in Solids*, McGraw Hill, New York, NY, 1969, p. 195.

18. D.W. MacLachlan, L.W. Wright, S.S.K. Gunturi, and D.M. Knowles: *Int. J. Plast.*, 2000, vol. 17, pp. 441 67.
19. D.W. MacLachlan, S.S.K. Gunturi, and D.M. Knowles: *Comp. Mater. Sci.*, 2002, vol. 25, pp. 129 41.
20. D.W. MacLachlan and D.M. Knowles: *Fatigue Fract. Eng. Mater. Struct.*, 2002, vol. 25, pp. 385 98.
21. D.W. MacLachlan and D.M. Knowles: *Fatigue Fract. Eng. Mater. Struct.*, 2002, vol. 25, pp. 399 409.
22. A. Ma, D. Dye, and R.C. Reed: *Acta Mater.*, 2008, vol. 56, pp. 1657 70.
23. H. Mecking and U.F. Kocks: *Acta Metall.*, 1981, vol. 29, pp. 1865 75.
24. Y. Estrin and H. Mecking: *Acta Metall.*, 1984, vol. 32, pp. 57 70.
25. B. Fedelich: *Int. J. Plast.*, 2002, vol. 18, pp. 1 49.
26. D. Peirce, R.J. Asaro, and A. Needleman: *Acta Metall.*, 1983, vol. 31, pp. 1951 76.
27. W. Schneider, J. Jammer, and H. Mughrabi H: *Superalloys 1992*, S.D. Antolovich, R.W. Stusrud, R.A. MacKay, D.L. Anton DL, T. Khan, R.D. Kissinger, and D.L. Klarstrom, eds., TMS, War rendale, PA, 1992, pp. 589 98.
28. W. Schneider and H. Mughrabi: *Creep and Fracture of Engineering Materials and Structures*, B. Wilshire and R.W. Evans, eds., Institute of Metals, London, UK, 1993, pp. 209 20.
29. H. Basoalto, S.K. Sondhi, B.F. Dyson, and M. McLean: *Super alloys 2004*, K.A. Green, T.M. Pollock, H. Harada, T.E. Howson, R.C. Reed, J.J. Schirra, and S. Walston, eds., TMS, Warrendale, PA, 2004, pp. 897 906.
30. U. Glatzel and M. Feller Kniepmeier: *Scripta Metall.*, 1991, vol. 25, pp. 1845 50.
31. J. Harder: *Int. J. Plast.*, 1999, vol. 15, pp. 605 24.
32. L. Tabourot, M. Fivel, and E. Rauch: *Mater. Sci. Eng. A*, 1997, vols. 234 236, pp. 639 42.
33. A. Arsenlis and D.M. Parks: *J. Mech. Phys. Solids*, 2002, vol. 50, pp. 1979 2009.
34. C.D. Allan: Ph.D. Dissertation, MIT, Cambridge, MA, 1995.